Geochemistry Geophysics Geosystems G3
AN ELECTRONIC JOURNAL OF THE EARTH SCIENCES
Published by AGU and the Geochemical Society

Article
Volume 10, Number 5
9 May 2009
Q05X06, doi:10.1029/2008GC002197
ISSN: 1525-2027

Click Here for Full Article

Peridotites from a ductile shear zone within back-arc lithospheric mantle, southern Mariana Trench: Results of a *Shinkai 6500* dive

K. Michibayashi
Institute of Geosciences, Shizuoka University, Shizuoka 422-8529, Japan (sekmich@ipc.shizuoka.ac.jp)

Y. Ohara
Hydrographic and Oceanographic Department of Japan, Tokyo 104-0045, Japan

Also at Institute for Research on Earth Evolution, Japan Agency for Marine-Earth Science and Technology, Kanagawa 236-0016, Japan.

R. J. Stern
Geosciences Department, University of Texas at Dallas, Richardson, Texas 75083, USA

P. Fryer
School of Earth Sciences and Technology, University of Hawai'i, Honolulu, Hawaii 96822, USA

J.-I. Kimura
Institute for Research on Earth Evolution, Japan Agency for Marine-Earth Science and Technology, Kanagawa 236-0016, Japan

M. Tasaka
Department of Earth and Planetary Sciences, University of Tokyo, Tokyo 113-0033, Japan

Y. Harigane
Frontier Science Organization, Kanazawa University, Kanazawa 920-1192, Japan

T. Ishii
Institute for Research on Earth Evolution, Japan Agency for Marine-Earth Science and Technology, Kanagawa 236-0016, Japan

[1] Two N–S fault zones in the southern Mariana fore arc record at least 20 km of left-lateral displacement. We examined the eastward facing slope of one of the fault zones (the West Santa Rosa Bank fault) from 6469 to 5957 m water depth using the submersible *Shinkai 6500* (YK06-12 Dive 973) as part of a cruise by the R/V *Yokosuka* in 2006. The dive recovered residual but still partly fertile lherzolite, residual lherzolite, and dunite; the samples show mylonitic, porphyroclastic, and coarse, moderately deformed secondary textures. Crystal-preferred orientations of olivine within the peridotites show a typical [100](010) pattern, with the fabric intensity decreasing from rocks with coarse secondary texture to mylonites. The sampled peridotites therefore represent a ductile shear zone within the lithospheric mantle of the overriding plate. Peridotites were probably exposed in association with a tear in the subducting slab, previously inferred from bathymetry and seismicity. Furthermore, although the dive site is located in the fore arc close to the Mariana Trench, spinel compositions within the sampled peridotites are comparable to those from the Mariana Trough back arc, suggesting that back-arc basin mantle is exposed along the West Santa Rosa Bank fault.

Copyright 2009 by the American Geophysical Union

Components: 9611 words, 9 figures, 7 tables.

Keywords: Mariana Trench; Mariana fore arc; Mariana Trough back-arc basin; peridotite; olivine CPO.

Index Terms: 8120 Tectonophysics: Dynamics of lithosphere and mantle: general (1213); 8170 Tectonophysics: Subduction zone processes (1031, 3060, 3613, 8413); 8159 Tectonophysics: Rheology: crust and lithosphere (8031).

Received 1 August 2008; **Revised** 9 March 2009; **Accepted** 17 March 2009; **Published** 9 May 2009.

Michibayashi, K., Y. Ohara, R. J. Stern, P. Fryer, J.-I. Kimura, M. Tasaka, Y. Harigane, and T. Ishii (2009), Peridotites from a ductile shear zone within back-arc lithospheric mantle, southern Mariana Trench: Results of a *Shinkai 6500* dive, *Geochem. Geophys. Geosyst.*, *10*, Q05X06, doi:10.1029/2008GC002197.

Theme: Izu-Bonin-Mariana Subduction System: A Comprehensive Overview Last
Guest Editors: Shuichi Kodaira, Sara Pozgay, and Jeffrey Ryan

1. Introduction

[2] The Mariana Trench is where the Pacific plate subducts beneath the Mariana plate [*Bird*, 2003]. The Challenger Deep, part of the southern Mariana Trench southwest of Guam, is the deepest trench in the world, and is up to 2 km deeper than the average of the Mariana Trench [*Fujioka et al.*, 2002; *Fryer et al.*, 2003]. The strike of the trench changes from N–S in the north to E–W in the south (Figure 1). The fore arc narrows markedly along the E-W segment (Figure 1) [*Stern and Smoot*, 1998]. It appears that the ~E-W opening of the Mariana Trough, coupled with a N-S tear in the slab beneath this region produced a narrow, shallow subducted slab to the west of the slab tear, which sinks more rapidly through the mantle than the wide, deep subducted slab to the east and north. It is this combination of circumstances that enables the slab to roll back, thereby explaining the great depth of the trench [*Fryer et al.*, 2003; *Gvirtzman and Stern*, 2004; *Miller et al.*, 2006], at the same time that it results in a remarkable amount of volcanic and tectonic activity in the overriding plate [*Martinez et al.*, 2000; *Kato et al.*, 2003].

[3] Large bathymetric gashes, inferred to represent fault zones, have been imaged by side-scan sonar in the fore arc west of Guam (Figure 1) [*Fryer et al.*, 2003]. For example, above the site where the N–S tear is thought to occur (i.e., beneath the fore arc immediately west of Guam), Santa Rosa Bank is bounded to the east by a N-S-striking left-lateral fault zone that records at least 20 km of displacement (Figure 1) [*Fryer et al.*, 2003]. Another fault to the west may be a sinistral strike-slip and/or normal fault related to opening of the Mariana Trough back-arc basin. The bathymetric youthfulness of these fault scarps suggests active tectonics and their location suggests they are associated with the inferred slab tear [*Fryer et al.*, 2003; *Gvirtzman and Stern*, 2004] and first motion solutions on earthquakes inferred to be within the subducting slab west of Santa Rosa Bank and near the trench show the left lateral strike-slip motion [*Fryer et al.*, 2003]. However, direct evidence for significant shearing deformation on the seafloor in this region, including geologic evidence, has yet to be reported.

[4] In this paper, we report results of studies of peridotites taken from the western wall of the West Santa Rosa Bank fault (Figure 1). In 2006, the submersible *Shinkai 6500* Dive 973 traversed ~2 km along the east facing slope of the bathymetric gash associate with the West Santa Rosa Bank fault, in water depths between 6469 m (12°14.5516′N, 144°07.8100′E) and 5957 m (12°14.9588′N, 144°06.8095′E [*Ohara et al.*, 2006]). An R/V *Yokosuka* bathymetric survey of the dive site (Figure 2) shows some variability in slope steepness along the track line. The slope exposes a variety of tectonized peridotites, including mylonites, suggesting that they formed in a ductile regime along the downdip extension of the fault, toward the slab tear. We show olivine fabric data and spinel mineral compositions and discuss implications for the tectonic affinity of the peridotites.

2. *Shinkai 6500* Dive 973 on the East Facing Scarp of the West Santa Rosa Bank Fault

[5] Dive observations began at the seafloor at 6469 m (Figure 2). We moved upslope westward,

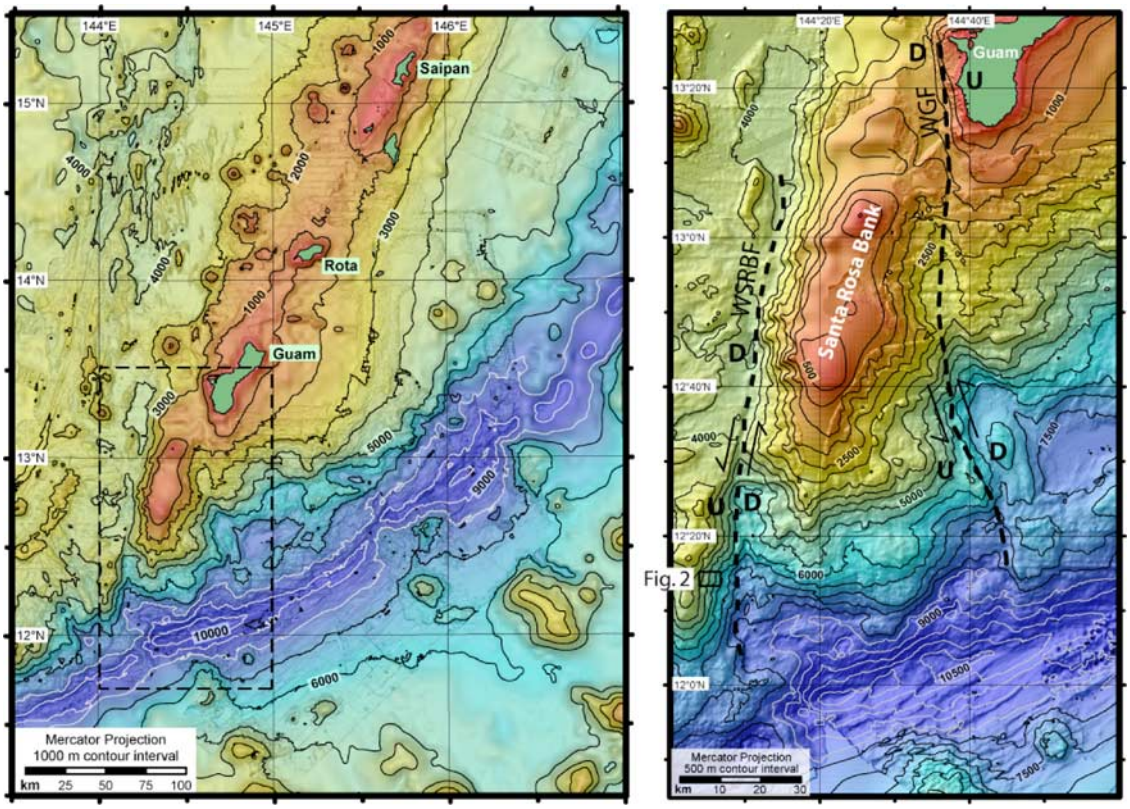

Figure 1. (left) Locality map of the southern Mariana arc and (right) enlargement showing the present study area (enlargement of the area within the dashed rectangle in Figure 1 (left), where the location of Figure 2 is shown). The data set used in each panel is a compilation of the following bathymetry data: (1) EM300 multibeam bathymetry, R/V *Thomas G. Thompson*, NOAA Ocean Exploration (OE) Submarine Ring of Fire (SRoF) 2003 (TN153) and 2004 (TN167) Cruises (contact is R. Embley); (2) SeaBat multibeam bathymetry, R/V *Natsushima*, JAMSTEC 2005 (NT0517) (contact is Y. Tamura) and JAMSTEC 2005 (NT0518) (contact is K. Nakamura); (3) SeaBeam 2000 multibeam bathymetry, R/V *Melville*, NOAA OE SRoF 2006 (MGLN02MV) (contact is R. Embley); (4) Cook07 Cruise 2001 (contacts are R. Stern and S. Bloomer); (5) SeaBeam 2100 multibeam bathymetry (50 m resolution), R/V *Onnuri*, NOAA OE Sounds of the Sea 2003 (contact is R. Dziak); (6) Hawaii Mapping Group H-MR1 surface-towed swath bathymetry, R/V *Melville*, Cook07 Cruise 2001 (contacts are R. Stern and S. Bloomer) and R/V *Moana Wave*, NSF 1997 (contacts are P. Fryer, F. Martinez, and N. Becker); (7) satellite altimetry data 1997 (contacts are W. Smith and D. Sandwell); and (8) SeaBeam 2112 bathymetry, R/V *Yokosuka*, YK06-12 Cruise 2006 [*Ohara et al.*, 2006] (contacts are Y. Ohara and R. Stern). Dashed lines in Figure 1 (right) represent the West Santa Rosa Bank fault (WSR BF) and the West Guam fault (WGF).

covering a total distance of ~1940 m and a vertical relief of 513 m (yielding an average seafloor slope of ~14.8°) and making five sampling stations (S1 to S5 in Figure 2). The material exposed on the scarp was mostly coarse angular talus, dominantly ~10–50 cm across but ranging to 1–3 m boulders. All the samples collected during Dive 973 are heavily altered peridotites.

[6] Near touchdown, we collected a cobble of moderately deformed peridotite (R1; S1 in Figure 2). Further upslope, at 6385 m depth in a sandy area, we collected two talus pieces (S2 in Figure 2): sample R2 is an intensely deformed mylonitic peridotite and R3 is a weakly to moderately deformed peridotite. At 6350 m, we traversed 100% exposure of coarse, angular to subangular debris of variable size, and collected five samples (R4–8 at 6355 m depth; S3 in Figure 2). R4, R5, and R7 are intensely deformed peridotite. R6 and R8 are weakly to moderately deformed peridotite. Outcrops occur from 6313 m to 6298 m depth. It is possible that the debris collected at deeper levels was derived from these outcrops or even shallower exposures.

[7] Large blocks/outcrops appeared at 6253 m, and another blocky talus deposit covered the slope starting at 6241 m depth. The talus blocks consisted of dark gray and dark green, angular to subangular, medium (<1 m) to large (>1 m) bould-

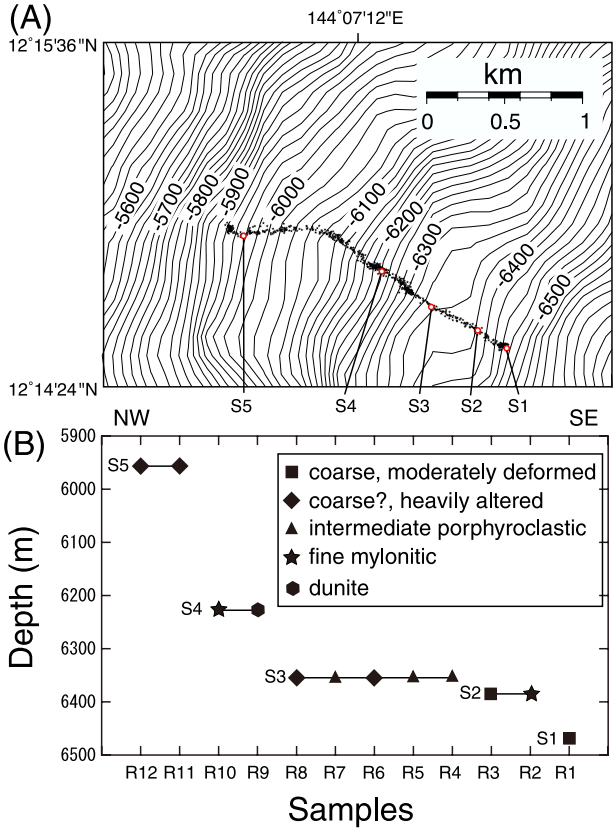

Figure 2. (a) Bathymetric map showing the dive track of the *Shinkai 6500* Dive 973 and sampling locations shown as S1–S5. The contour interval is 20 m. The small star symbols that define the dive track show the submersible location at 5-min intervals. (b) Sampling depth versus microstructure of recovered samples. Symbols correspond to petrographic character in the enclosed box and are used in Figures 6–9.

ers. Two samples of coarse talus were collected at 6228 m depth (S4 in Figure 2): R9 is a dunite and R10 is a mylonitic peridotite. The coarse talus slope ended at 6185 m. Above this, the slope was covered with numerous cobbles and boulders. Two samples of weakly deformed peridotite were collected from this talus at 5957 m (R11–12; S5 in Figure 2).

3. Peridotites From the West Santa Rosa Bank Fault

3.1. Petrography

[8] Foliation and lineation were identified based solely on the alignment of spinel and pyroxene grains (even within the heavily altered samples), as observed in the laboratory from bleached and saw cut samples [e.g., *Michibayashi*, 2008]. We analyzed microstructures in all samples from thin sections cut perpendicular to the foliation and parallel to the lineation (i.e., XZ sections). On the basis of these analyses, we classified the peridotites shown in Figure 2b into three microstructural categories: coarse- to intermediate-grained moderately deformed rocks, intermediate to fine-grained porphyroclastic rocks, and fine-grained mylonitic rocks, as follows:

[9] Coarse- to intermediate-grained, moderately deformed peridotites are represented by R1 and R3 (Figures 2b and 3). These samples consist dominantly of relatively coarse olivine grains of up to several millimeters, although they are partly recrystallized to intermediate-sized grains several hundred microns across. Orthopyroxenes have irregular grain boundaries and are elongate, defining the foliation and lineation. Four other samples (R6, R8, R11, and R12) also possess similarly coarse-grained, inhomogeneous textures; however, olivines in these samples are so heavily altered that it is difficult to identify the textures in detail.

[10] The group of intermediate- to fine-grained porphyroclastic peridotites includes samples R4, R5, and R7 (Figures 2b and 3). These are characterized by orthopyroxene porphyroclasts, several millimeters across, within a matrix of intermediate-sized olivine grains, several hundred microns across. Orthopyroxene porphyroclasts are either rounded or intensely elongated with irregular grain boundaries. In particular, olivines in sample R5 are relatively fine (tens to several hundreds of microns).

[11] Mylonitic peridotites include samples R2 and R10 (Figures 2b and 3). These rocks are characterized by relatively small and rounded orthopyroxene compared with those in the porphyroclastic peridotites. In particular, R2 consists of alternating very fine-grained (several microns across) layers and intermediate-grained (several hundred microns) layers. The very fine-grained areas in R2 are characteristic of ultramylonite. R10 shows similar textural variations; however, the sample is too altered to identify its microstructure in greater detail.

[12] R9 is a heavily altered dunite (Figures 2b and 3). Despite the alteration, individual olivines can be recognized from extinction patterns in cross-polarized light. The olivines range in size from fine (several tens of microns) to intermediate (several hundreds of microns; Figure 3).

[13] Every sample except dunite (R9) includes minor clinopyroxene. Since clinopyroxenes are generally small (approximately one hundred

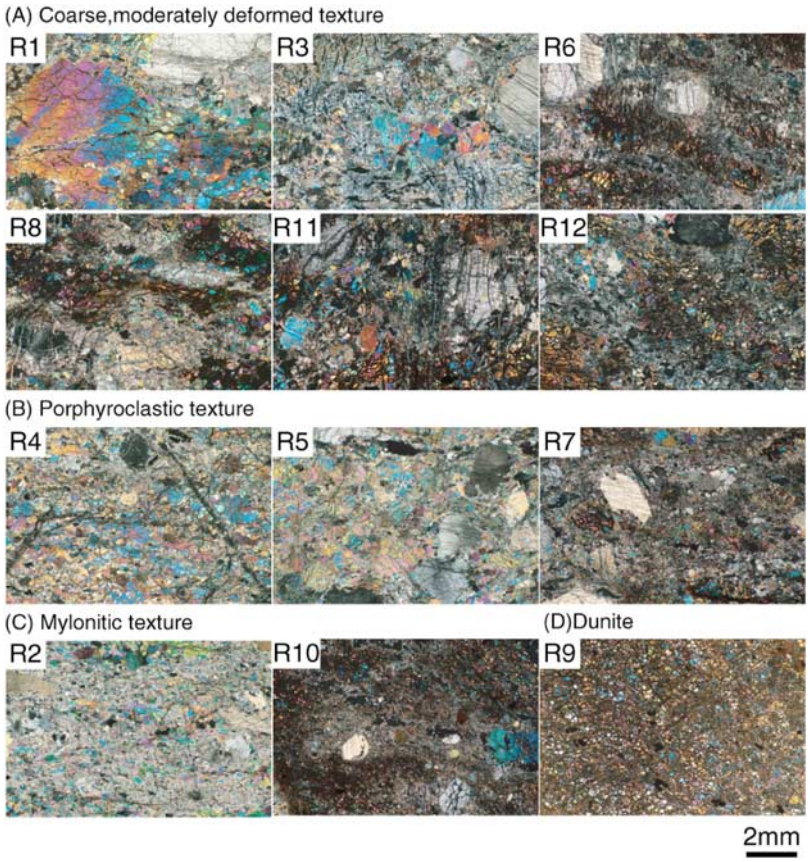

Figure 3. Microphotographs (cross-polarized light) of peridotites collected during *Shinkai 6500* Dive 973. (a) Coarse- to intermediate-grained, moderately deformed texture: R1 and R3. Heavily altered samples (coarse- to intermediate-grained, moderately deformed textures?): R6, R8, R11, and R12. (b) Intermediate- to fine-grained porphyroclastic textures: R4, R5, and R7. (c) Fine-grained mylonitic textures: R2 and R10. (d) Heavily altered dunite: R9.

microns) and samples suffer variable alteration, it is sometimes difficult to distinguish clinopyroxene from orthopyroxene. Every sample except dunite (R9) also includes plagioclase that appears as fresh interstitial grains or altered phases as irregular diffuse dark brown patches of hydrogrossular (e.g., Figure 4).

3.2. Olivine Fabrics

[14] To examine the deformation conditions in detail, we measured the crystal-preferred orientations (CPO) of olivine. We determined between 97 and 218 olivine crystal orientations per sample (Figure 5), and visually checked the computerized indexation of the diffraction pattern for each orientation.

[15] Fabric strength and the distribution density of the principal crystallographic axes characterize the CPO [e.g., *Michibayashi and Mainprice*, 2004]. The rotation matrix between crystal and sample coordinates defines the orientation, **g**, of a crystal in sample coordinates. In practice, it is convenient

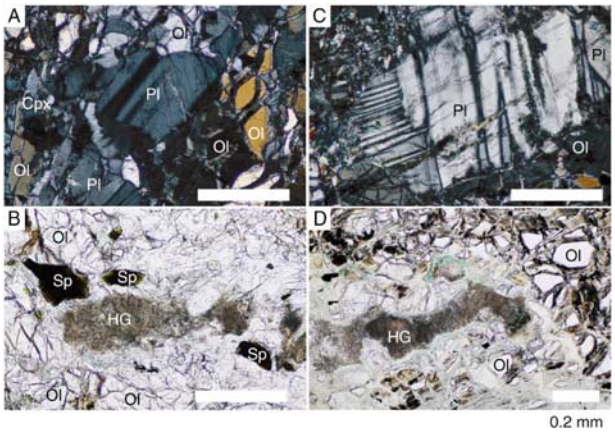

Figure 4. Photomicrographs of Dive 973 peridotites showing habits of plagioclase and its altered phase. (a) Fresh interstitial plagioclase associated with olivine and clinopyroxene in R4. Cross-polarized light. (b) Hydrogrossular associated with spinel and olivine in R4. Plane-polarized light. (c) Fresh interstitial plagioclase associated with olivine in R12. Cross-polarized light. (d) Hydrogrossular associated with olivine in R12. Plane-polarized light. Pl, plagioclase; HG, hydrogrossular; Ol, olivine; Cpx, clinopyroxene; Sp, spinel.

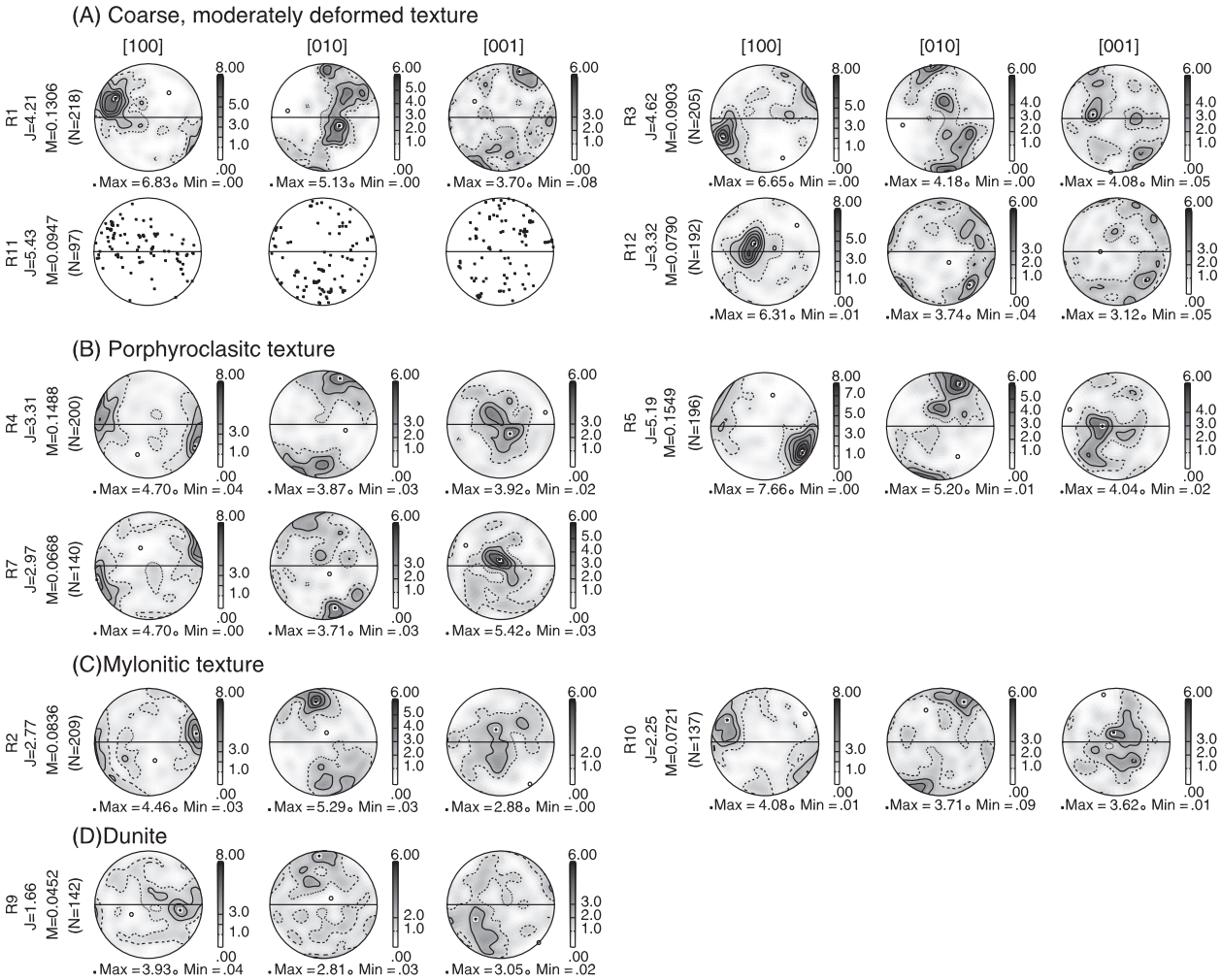

Figure 5. Stereoplots showing olivine crystal-preferred orientation data measured from highly polished thin sections using a scanning electron microscope equipped with an electron-backscatter diffraction system, housed at the Center for Instrumental Analysis, Shizuoka University, Japan [e.g., *Michibayashi et al.*, 2006b, 2007; *Harigane et al.*, 2008; *Tasaka et al.*, 2008]. (a) Coarse, moderately deformed texture: R1. Intensely serpentinized samples (coarse, moderately deformed textures?): R3, R11, and R12. (b) Porphyroclastic textures: R4, R5, and R7. (c) Mylonitic textures: R2 and R10. (d) Intensely serpentinized dunite: R9. Contours are multiples of uniform distribution. Foliation is horizontal, and lineation is E–W. *J* index and *M* index are the fabric intensities calculated after *Mainprice et al.* [2000] and *Skemer et al.* [2005], respectively.

to describe the rotation by a triplet of Euler angles; for example, $\mathbf{g} = (\varphi_1, \varphi, \varphi_2)$, as used by *Bunge* [1982]. The orientation distribution function, f(**g**), is defined as the volume fraction of orientations with an orientation in the interval between **g** and **g** + d**g** in a space containing all possible orientations, given by $\Delta V/V = \int f(\mathbf{g})\, d\mathbf{g}$ where $\Delta V/V$ is the volume fraction of crystals with orientation **g**, f(**g**) is the texture function, and $d\mathbf{g} = 1/8\pi^2 \sin\varphi d\varphi_1 d\varphi d\varphi_2$ is the volume of the region of integration in orientation space. We use the *J* index [*Mainprice and Silver*, 1993] to quantify the intensity of a given CPO, where $J = \int f(\mathbf{g})^2\, d\mathbf{g}$. The *J* index has a value of 1 for randomly oriented crystals and infinity for a single crystal. The *J* index for olivine in our calculations has a maximum of ~250 because of the truncation of the spherical harmonic series at an expansion of 22.

[16] The fabric strength was also determined using the M index technique [*Skemer et al.*, 2005]. In the M index technique, the distribution of a sample's random pair misorientation angles [*Wheeler et al.*, 2001] is compared to a distribution of misorientation angles from a theoretical random fabric. The M index is scaled from zero to one, where M = 0 represents a random fabric and M = 1 represents a single crystal.

[17] Measured olivine CPOs vary between coarse, moderately deformed peridotites and the other

Table 1. Electron Probe Analyses of Olivine of Dive 973 Peridotites[a]

	Sample Number											
	R01	R02	R03	R04	R05	R06	R07	R08	R09	R10	R11	R12
No. anal.	10	6	10	11	11	9	13	10	8	9	9	9
SiO_2	41.03	40.91	40.88	40.85	40.91	40.86	41.00	41.02	40.55	40.70	40.88	41.04
TiO_2	0.01	0.05	0.02	0.01	0.03	0.02	0.02	0.03	0.01	0.03	0.03	0.03
Al_2O_3	0.01	0.00	0.01	0.01	0.01	0.00	0.01	0.01	0.00	0.01	0.01	0.01
FeO	8.95	9.25	9.69	9.46	9.50	8.84	9.07	8.88	8.71	9.49	9.44	9.26
MnO	0.11	0.12	0.16	0.15	0.16	0.11	0.14	0.13	0.15	0.14	0.15	0.15
MgO	50.88	50.33	50.02	50.21	50.34	50.28	50.41	50.42	50.22	50.04	50.27	50.46
CaO	0.03	0.01	0.02	0.01	0.02	0.02	0.02	0.03	0.02	0.01	0.03	0.02
Na_2O	0.01	0.01	0.01	0.00	0.01	0.01	0.00	0.00	0.01	0.01	0.01	0.00
K_2O	0.01	0.01	0.00	0.01	0.01	0.00	0.00	0.00	0.00	0.01	0.01	0.01
Cr_2O_3	0.01	0.00	0.01	0.01	0.01	0.01	0.01	0.00	0.00	0.01	0.01	0.01
V_2O_3	0.01	0.01	0.00	0.01	0.01	0.01	0.01	0.00	0.01	0.01	0.01	0.01
NiO	0.42	0.42	0.41	0.41	0.39	0.42	0.41	0.40	0.37	0.37	0.39	0.41
P_2O_5	0.00	0.02	0.01	0.01	0.01	0.01	0.01	0.01	0.01	0.02	0.00	0.00
Total	101.48	101.14	101.24	101.15	101.42	100.60	101.12	100.93	100.07	100.84	101.24	101.41
Cations												
Si	5.93	5.94	5.95	5.94	5.94	5.96	5.95	5.96	5.94	5.94	5.94	5.95
Ti	0.00	0.01	0.00	0.00	0.00	0.00	0.00	0.00	0.00	0.00	0.00	0.00
Al	0.00	0.00	0.00	0.00	0.00	0.00	0.00	0.00	0.00	0.00	0.00	0.00
Fe	1.08	1.12	1.18	1.15	1.15	1.08	1.10	1.08	1.07	1.16	1.15	1.12
Mn	0.01	0.01	0.02	0.02	0.02	0.01	0.02	0.02	0.02	0.02	0.02	0.02
Mg	10.97	10.90	10.85	10.89	10.89	10.93	10.91	10.92	10.97	10.88	10.89	10.90
Ca	0.00	0.00	0.00	0.00	0.00	0.00	0.00	0.00	0.00	0.00	0.00	0.00
Na	0.00	0.00	0.00	0.00	0.00	0.00	0.00	0.00	0.00	0.00	0.00	0.00
K	0.00	0.00	0.00	0.00	0.00	0.00	0.00	0.00	0.00	0.00	0.00	0.00
Cr	0.00	0.00	0.00	0.00	0.00	0.00	0.00	0.00	0.00	0.00	0.00	0.00
V	0.00	0.00	0.00	0.00	0.00	0.00	0.00	0.00	0.00	0.00	0.00	0.00
Ni	0.05	0.05	0.05	0.05	0.05	0.05	0.05	0.05	0.04	0.04	0.05	0.05
P	0.00	0.00	0.00	0.00	0.00	0.00	0.00	0.00	0.00	0.00	0.00	0.00
O	24.00	24.00	24.00	24.00	24.00	24.00	24.00	24.00	24.00	24.00	24.00	24.00
Total	18.06	18.05	18.05	18.06	18.06	18.04	18.04	18.04	18.06	18.06	18.06	18.05
Mg #	0.91	0.91	0.90	0.90	0.90	0.91	0.91	0.91	0.91	0.90	0.90	0.91
1σ	0.003	0.001	0.002	0.002	0.002	0.003	0.002	0.001	0.001	0.002	0.001	0.001

[a] Average compositions. Unit is wt %. No. anal., number of analyses making up the average composition.

samples (Figure 5). We excluded two samples from analysis (R6 and R8) because we considered it sufficient to measure just two of the heavily altered samples (R11 and R12). Among the 10 measured samples, 5 clearly show a typical [100](010) pattern: R2, R4, R5, R7, and R10. In this fabric, [100] is subparallel to the lineation, [010] normal to the foliation, and [001] normal to lineation within the plane of the foliation (Figure 5). These five samples include both porphyroclastic and mylonitic peridotites, emphasizing the gradational nature of these categories. With respect to the fabric intensity, the highest value is $J = 5.19$ in R5 (M = 0.1549 in R5), and the lowest is $J = 2.25$ in R10 (M = 0.0668 in R7).

[18] The coarse, moderately deformed peridotites show variable olivine CPO patterns (Figure 5) [e.g., *Mainprice*, 2007; *Karato*, 2008; *Michibayashi*, 2008]. R1 possibly shows a [100](001) pattern, although [010] has a girdle distribution normal to the lineation. R3 possibly shows a [100](010) pattern, although [001] has a range of orientations, with no clear concentration. In R11, [100] shows a girdle distribution with a maximum density subparallel to the lineation, whereas both [010] and [001] have maximum densities subnormal to the foliation. The CPO pattern in R12 shows a [100]{0kl} pattern, although [100] is oblique to the lineation by 50°.

[19] The CPO pattern in the dunite (R9) is very weak. Its fabric intensity is as low as $J = 1.66$ (M = 0.0452). However, the area of highest density for each axis may represent a weak [100](010) pattern (Figure 5).

3.3. Mineral Chemistry

[20] The compositions of constituent minerals (olivine, orthopyroxene, clinopyroxene, spinel and

Table 2. Electron Probe Analyses of Orthopyroxene of Dive 973 Peridotites[a]

	Sample Number										
	R01	R02	R03	R04	R05	R06	R07	R08	R10	R11	R12
No. anal.	10	14	10	8	7	11	7	9	10	10	10
SiO_2	55.91	56.55	55.86	55.67	56.06	56.58	55.96	55.51	56.05	55.69	56.37
TiO_2	0.14	0.11	0.19	0.10	0.16	0.13	0.14	0.10	0.12	0.16	0.13
Al_2O_3	3.00	2.44	2.47	3.98	2.66	2.65	3.18	3.81	2.75	3.39	2.65
FeO	6.04	6.02	6.35	6.01	6.30	6.17	6.20	5.92	6.36	6.16	6.11
MnO	0.15	0.16	0.17	0.15	0.16	0.14	0.17	0.15	0.16	0.17	0.14
MgO	34.04	34.51	33.65	33.48	33.72	34.52	34.25	33.50	33.72	33.05	34.04
CaO	0.78	0.57	0.88	1.00	1.17	0.51	0.48	0.93	0.99	1.45	1.15
Na_2O	0.01	0.01	0.03	0.02	0.02	0.00	0.01	0.03	0.02	0.03	0.02
K_2O	0.00	0.00	0.01	0.00	0.01	0.01	0.01	0.00	0.01	0.00	0.00
Cr_2O_3	0.73	0.47	0.60	0.60	0.67	0.45	0.55	0.64	0.44	0.69	0.75
V_2O_3	0.02	0.02	0.03	0.02	0.01	0.02	0.02	0.02	0.02	0.02	0.02
NiO	0.09	0.08	0.09	0.10	0.09	0.08	0.07	0.10	0.09	0.08	0.11
P_2O_5	0.00	0.01	0.01	0.00	0.00	0.00	0.01	0.01	0.01	0.01	0.01
Total	100.93	100.94	100.33	101.14	101.03	101.27	101.07	100.71	100.72	100.90	101.51
Cations											
Si	7.66	7.73	7.71	7.61	7.69	7.72	7.66	7.62	7.70	7.65	7.69
Ti	0.01	0.01	0.02	0.01	0.02	0.01	0.01	0.01	0.01	0.02	0.01
Al	0.49	0.39	0.40	0.64	0.43	0.43	0.51	0.62	0.45	0.55	0.43
Fe	0.69	0.69	0.73	0.69	0.72	0.70	0.71	0.68	0.73	0.71	0.70
Mn	0.02	0.02	0.02	0.02	0.02	0.02	0.02	0.02	0.02	0.02	0.02
Mg	6.96	7.04	6.93	6.83	6.90	7.02	6.99	6.86	6.91	6.77	6.92
Ca	0.12	0.08	0.13	0.15	0.17	0.07	0.07	0.14	0.15	0.22	0.17
Na	0.00	0.00	0.01	0.01	0.01	0.00	0.00	0.01	0.00	0.01	0.01
K	0.00	0.00	0.00	0.00	0.00	0.00	0.00	0.00	0.00	0.00	0.00
Cr	0.08	0.05	0.07	0.06	0.07	0.05	0.06	0.07	0.05	0.08	0.08
V	0.00	0.00	0.00	0.00	0.00	0.00	0.00	0.00	0.00	0.00	0.00
Ni	0.01	0.01	0.01	0.01	0.01	0.01	0.01	0.01	0.01	0.01	0.01
P	0.00	0.00	0.00	0.00	0.00	0.00	0.00	0.00	0.00	0.00	0.00
O	24.00	24.00	24.00	24.00	24.00	24.00	24.00	24.00	24.00	24.00	24.00
Total	16.04	16.03	16.03	16.03	16.04	16.03	16.04	16.03	16.04	16.02	16.04
Mg #	0.91	0.91	0.90	0.91	0.91	0.91	0.91	0.91	0.90	0.91	0.91
1σ	0.002	0.003	0.002	0.002	0.003	0.001	0.001	0.002	0.003	0.003	0.001
Brey and Köhler [1990] OPX thermometer											
P (kb)	10	10	10	10	10	10	10	10	10	10	10
T (°C)	968	900	998	1026	1067	875	866	1009	1024	1128	1062

[a] Average compositions. Unit is wt %. Estimated temperatures calculated after *Brey and Köhler* [1990]. No. anal., number of analyses making up the average composition.

plagioclase) (Tables 1–3, 4a, 4b, and 5) were determined using a JEOL JCXA-733 electron microprobe at the Ocean Research Institute of the University of Tokyo, Japan using accelerating voltage, 15 kV; specimen current, 12 nA; beam diameter, 1 μm; and using correction procedures after *Bence and Albee* [1968]. The Fe^{3+} content of spinel was calculated on the basis of stoichiometry.

[21] Plots of the atomic Cr/(Cr + Al) ratio (=Cr #) (Figure 6a), Mg/(Mg + Fe) ratio (=Mg #) (Figure 6b) and TiO_2 wt % (Figure 6c) of spinel show considerable ranges but no systematic geographic trends are apparent. All samples contain moderately high-Cr # spinels (up to 0.51 in R5 and R12; Figure 6a); however, four samples (R4, R7, R8, and R11) also contain some relatively low-Cr # spinels (as low as 0.18 in R4), defining a bimodal distribution. We define Cr # = 0.25 as an arbitrary boundary separating low-Cr # and high-Cr # spinels (Figures 6 and 7).

[22] Cr # for Dive 973 peridotite spinels range from low values like those of the Parece Vela Basin [*Ohara et al.*, 2003] and Mariana Trough [*Ohara et al.*, 2002] to high values of the Mariana fore arc (landward slope of the Mariana Trench [*Ohara and Ishii*, 1998]) (Figure 7). The first two are representative of Neogene back-arc basin peridotite spinels and record minor to moderate degrees of mantle depletion, similar to that of abyssal (mid-ocean ridge) peridotites. In contrast, Mariana fore-arc

Table 3. Electron Probe Analyses of Clinopyroxene of Dive 973 Peridotites[a]

	Sample Number										
	R01	R02	R03	R04	R05	R06	R07	R08	R10	R11	R12
No. anal.	11	10	10	10	9	10	10	10	10	15	10
SiO_2	52.29	51.98	52.01	52.65	52.59	53.33	52.66	52.11	52.11	52.22	52.64
TiO_2	0.41	0.58	0.68	0.45	0.58	0.37	0.45	0.41	0.43	0.48	0.39
Al_2O_3	4.62	4.48	3.93	3.90	3.66	3.18	3.67	5.06	4.08	3.99	3.61
FeO	2.30	2.48	2.76	2.40	2.64	2.25	2.63	2.44	2.47	2.51	2.28
MnO	0.07	0.07	0.13	0.10	0.07	0.07	0.08	0.06	0.08	0.10	0.07
MgO	17.10	16.43	16.10	16.62	16.19	16.80	16.46	16.11	16.35	16.10	16.62
CaO	20.91	22.12	22.88	22.88	23.02	23.81	23.00	22.73	23.24	23.06	22.87
Na_2O	0.71	0.82	0.57	0.53	0.51	0.32	0.47	0.57	0.33	0.42	0.48
K_2O	0.00	0.01	0.00	0.01	0.00	0.01	0.01	0.00	0.00	0.01	0.00
Cr_2O_3	1.31	1.20	1.20	0.98	1.15	0.88	0.81	1.16	0.92	1.13	1.28
V_2O_3	0.04	0.05	0.06	0.05	0.05	0.05	0.04	0.03	0.05	0.06	0.06
NiO	0.04	0.06	0.04	0.06	0.06	0.05	0.07	0.04	0.05	0.04	0.05
P_2O_5	0.02	0.03	0.02	0.02	0.03	0.03	0.02	0.02	0.03	0.02	0.02
Total	99.83	100.31	100.39	100.64	100.55	101.13	100.36	100.75	100.15	100.14	100.36
Cations											
Si	7.58	7.54	7.56	7.61	7.62	7.67	7.64	7.52	7.58	7.60	7.63
Ti	0.04	0.06	0.07	0.05	0.06	0.04	0.05	0.04	0.05	0.05	0.04
Al	0.79	0.77	0.67	0.67	0.62	0.54	0.63	0.86	0.70	0.68	0.62
Fe	0.28	0.30	0.34	0.29	0.32	0.27	0.32	0.29	0.30	0.31	0.28
Mn	0.01	0.01	0.02	0.01	0.01	0.01	0.01	0.01	0.01	0.01	0.01
Mg	3.69	3.55	3.49	3.58	3.50	3.60	3.56	3.47	3.54	3.49	3.59
Ca	3.25	3.44	3.57	3.54	3.57	3.67	3.57	3.51	3.62	3.59	3.55
Na	0.20	0.23	0.16	0.15	0.14	0.09	0.13	0.16	0.09	0.12	0.13
K	0.00	0.00	0.00	0.00	0.00	0.00	0.00	0.00	0.00	0.00	0.00
Cr	0.15	0.14	0.14	0.11	0.13	0.10	0.09	0.13	0.11	0.13	0.15
V	0.01	0.01	0.01	0.01	0.01	0.01	0.00	0.00	0.01	0.01	0.01
Ni	0.01	0.01	0.00	0.01	0.01	0.01	0.01	0.00	0.01	0.01	0.01
P	0.00	0.00	0.00	0.00	0.00	0.00	0.00	0.00	0.00	0.00	0.00
O	24.00	24.00	24.00	24.00	24.00	24.00	24.00	24.00	24.00	24.00	24.00
Total	16.00	16.05	16.03	16.02	16.00	16.01	16.01	16.01	16.01	16.00	16.01
Mg #	0.93	0.92	0.91	0.92	0.92	0.93	0.92	0.92	0.92	0.92	0.93
1σ	0.006	0.007	0.007	0.007	0.007	0.008	0.018	0.005	0.004	0.008	0.009

[a] Average compositions. Unit is wt %. No. anal., number of analyses making up the average composition.

peridotite spinels reflect unusually high degrees of melting, interpreted to accompany formation of a new subduction zone during Eocene time. Although some overlap with fore-arc peridotite spinels is seen, the Dive 973 peridotite spinels are mostly similar to those of back-arc basins.

3.4. Bulk Rock Chemistry

[23] For analyses of bulk rock chemistry (Table 6), samples were crushed manually in an iron pestle, rinsed with distilled water in an ultrasonic bath, and dried for 2 h at 110°C. Dried chips were then ground in an agate mortar for 30 min. The resulting powder was ignited at 1100°C for 3 h. Glass disks with a flux:sample ratio of 2:1 were prepared following the method of *Kimura and Yamada* [1996]. The disks were then analyzed for major and minor elements at Shimane University, Japan, using a Rigaku RIX 2000 wavelength dispersive X-ray fluorescence (XRF) spectrometer. We used CaO-Al_2O_3 relations to assess the relative depletion of Dive 973 peridotites, because the abundance of these oxides decreases as melt depletion increases. A $CaO-Al_2O_3$ plot for bulk rocks analyzed in this study (Figure 8) shows that they contain significantly more CaO and Al_2O_3 and fall outside of the field of the Mariana fore-arc (serpentinite diapir seamounts) peridotites of *Ishii et al.* [1992] and follow a mantle depletion trend [e.g., *Ishiwatari*, 1985].

[24] Mineral modes of primary phases were calculated using a least squares mass balance of the bulk rock and mineral compositions by the method adopted by *Takazawa et al.* [2003], since it is so difficult to provide modal composition by a point-counting method because of small grain sizes of clinopyroxene and plagioclase, and overall alter-

Table 4a. Electron Probe Analyses of Spinel of Dive 973 Peridotites[a]

	Sample Number							
	R01	R02	R03	R05	R06	R09	R10	R12
No. anal.	10	10	4	13	5	11	10	10
SiO_2	0.02	0.03	0.02	0.03	0.06	0.00	0.01	0.02
TiO_2	0.50	0.26	0.49	0.58	0.24	0.25	0.24	0.38
Al_2O_3	29.98	34.13	26.63	29.15	34.52	35.69	37.77	28.28
FeO	17.86	15.32	18.19	17.24	15.98	15.16	15.29	17.68
Fe_2O_3	3.72	2.80	4.34	5.21	3.53	4.42	3.17	3.91
MnO	0.29	0.26	0.25	0.29	0.26	0.22	0.23	0.28
MgO	12.65	14.44	11.88	12.83	14.09	14.71	14.72	12.38
CaO	0.01	0.01	0.02	0.01	0.02	0.01	0.01	0.01
Cr_2O_3	34.16	31.92	36.50	33.12	30.66	29.11	27.47	36.03
V_2O_3	0.22	0.22	0.33	0.31	0.20	0.20	0.18	0.27
NiO	0.18	0.17	0.16	0.20	0.16	0.20	0.20	0.16
Total	99.58	99.56	98.80	98.96	99.71	99.97	99.30	99.41
Cations								
Si	0.00	0.00	0.00	0.00	0.00	0.00	0.00	0.00
Ti	0.01	0.01	0.01	0.01	0.01	0.01	0.01	0.01
Al	1.07	1.18	0.97	1.05	1.19	1.22	1.29	1.02
Fe^{2+}	0.43	0.36	0.45	0.42	0.38	0.36	0.36	0.43
Fe^{3+}	0.08	0.06	0.10	0.11	0.08	0.09	0.07	0.09
Mn	0.01	0.01	0.01	0.01	0.01	0.01	0.01	0.01
Mg	0.57	0.63	0.55	0.58	0.62	0.64	0.63	0.56
Ca	0.00	0.00	0.00	0.00	0.00	0.00	0.00	0.00
Cr	0.82	0.74	0.90	0.80	0.71	0.67	0.63	0.87
V	0.01	0.01	0.01	0.01	0.00	0.00	0.00	0.01
Ni	0.00	0.00	0.00	0.00	0.00	0.00	0.00	0.00
O	4.00	4.00	4.00	4.00	4.00	4.00	4.00	4.00
Total	3.00	3.00	3.00	3.00	3.00	3.00	3.00	3.00
Mg #	0.57	0.63	0.55	0.58	0.62	0.64	0.64	0.56
1σ	0.05	0.02	0.01	0.03	0.02	0.02	0.04	0.04
Cr #	0.434	0.386	0.479	0.433	0.374	0.354	0.330	0.462
1σ	0.031	0.011	0.030	0.046	0.009	0.026	0.059	0.034
Cr # max	0.477	0.403	0.501	0.508	0.385	0.382	0.447	0.508
Cr # min	0.384	0.366	0.436	0.312	0.362	0.294	0.262	0.405

[a] Average compositions. Unit is wt %. No. anal., number of analyses making up the average composition.

ation of the samples. The calculation was performed by fitting mineral compositions to bulk rock compositions in terms of SiO_2, Al_2O_3, FeO, MgO, CaO, Na_2O, Cr_2O_3 and NiO content. We use the calculated modes for defining rocks type; for example, lherzolite is peridotite with modal clinopyroxene greater than 5%. The result shows that the peridotites in this study are mostly lherzolites (Table 6).

4. Interpretation and Discussion

4.1. Development of a Ductile Shear Zone Beneath the West Santa Rosa Bank Fault

[25] Our microstructure data show that in general, the coarse-grained granular textures indicate deformation at near-solidus or hypersolidus temperatures, typical of asthenospheric flow; these are therefore interpreted as primary mantle textures, whereas the finer-grained textures (porphyroclastic and mylonitic textures) reflect ductile flow at lower temperatures [e.g., *Nicolas and Poirier*, 1976; *Michibayashi and Mainprice*, 2004]. Although 6 of the 12 samples analyzed in this study show relatively coarse-grained textures, olivine grains in these samples are remarkably elongate, show intense undulose extinction, and are partly dynamically recrystallized to intermediate sizes (Figure 3). These features indicate that the grains were inhomogeneously deformed under relatively low-temperature conditions. It is therefore likely that all of the recovered peridotites contain secondary textures, presumably representing deformation within relatively cold lithospheric mantle [e.g., *Drury et al.*, 1991; *Jaroslow et al.*, 1996; *Newman et al.*, 1999; *Dijkstra et al.*, 2002; *Michibayashi and Mainprice*, 2004; *Harigane et al.*, 2005; *Michibayashi et al.*, 2006a; *Warren and Hirth*, 2006; *Warren et al.*, 2008; *Webber et al.*, 2008].

Table 4b. Electron Probe Analyses of Spinel of Dive 973 Peridotites[a]

	Sample Number							
	R4		R07		R08		R11	
	Cr # > 0.25	Cr # < 0.25	Cr # > 0.25	Cr # < 0.25	Cr # > 0.25	Cr # < 0.25	Cr # > 0.25	Cr # < 0.25
No. anal.	4	8	5	6	3	6	13	2
SiO_2	0.02	0.01	0.01	0.01	0.04	0.04	0.04	0.02
TiO_2	0.31	0.05	0.30	0.17	0.29	0.14	0.58	0.36
Al_2O_3	25.56	49.35	37.31	45.62	33.71	46.78	31.57	45.43
FeO	20.86	11.82	14.13	11.89	17.87	12.10	16.33	12.92
Fe_2O_3	10.39	2.76	2.42	2.32	2.12	2.47	4.87	3.57
MnO	0.40	0.13	0.19	0.17	0.26	0.18	0.23	0.17
MgO	9.78	17.91	15.58	17.60	12.70	17.50	13.92	17.40
CaO	0.01	0.01	0.01	0.01	0.01	0.01	0.01	0.02
Cr_2O_3	30.96	16.76	29.08	20.78	31.62	19.09	31.91	20.14
V_2O_3	0.23	0.09	0.19	0.15	0.17	0.10	0.26	0.19
NiO	0.20	0.33	0.20	0.27	0.14	0.28	0.22	0.33
Total	98.72	99.20	99.44	98.98	98.92	98.68	99.94	100.55
Cations								
Si	0.00	0.00	0.00	0.00	0.00	0.00	0.00	0.00
Ti	0.01	0.00	0.01	0.00	0.01	0.00	0.01	0.01
Al	0.91	1.58	1.27	1.49	1.19	1.52	1.11	1.47
Fe^{2+}	0.57	0.27	0.33	0.27	0.43	0.27	0.38	0.28
Fe^{3+}	0.29	0.06	0.05	0.05	0.05	0.05	0.10	0.07
Mn	0.01	0.00	0.00	0.00	0.01	0.00	0.01	0.00
Mg	0.44	0.72	0.67	0.73	0.57	0.72	0.62	0.71
Ca	0.00	0.00	0.00	0.00	0.00	0.00	0.00	0.00
Cr	0.77	0.36	0.66	0.45	0.75	0.42	0.76	0.44
V	0.01	0.00	0.00	0.00	0.00	0.00	0.01	0.00
Ni	0.01	0.00	0.00	0.01	0.00	0.01	0.01	0.01
O	4.00	4.00	4.00	4.00	4.00	4.00	4.00	4.00
Total	3.02	3.00	3.00	3.00	3.00	3.00	3.00	3.00
Mg #	0.44	0.73	0.67	0.73	0.57	0.73	0.62	0.72
1σ	0.23	0.02	0.03	0.01	0.06	0.01	0.03	0.01
Cr #	0.498	0.186	0.344	0.234	0.386	0.215	0.406	0.230
1σ	0.189	0.007	0.023	0.013	0.018	0.009	0.063	0.023
Cr # max	0.780	0.198	0.373	0.249	0.403	0.225	0.458	0.246
Cr # min	0.379	0.179	0.312	0.211	0.367	0.204	0.274	0.213

[a]For those including low-Cr #; average compositions. Unit is wt %. No. anal., number of analyses making up the average composition.

[26] The distribution of the 12 peridotite samples from the five sites (Figures 2 and 9a) shows that intense shear deformation, resulting in the formation of mylonitic peridotites (stars in S2 and S4), is localized within a horizontal interval of approximately 800 m (Figure 9a). Porphyroclastic peridotites (triangles) were found within this interval at S3, between S2 and S4 where the mylonitic peridotites were found (Figure 9a). Olivine fabric intensity decreases toward S4 (Figure 9b), where the mylonitic peridotite was found. *Michibayashi et al.* [2006a] reported that olivine fabric intensity decreased toward to the center of a shear zone within the Fizh mantle section of the Oman ophiolite, as a result of grain size reduction processes. In this context, the data in Figures 9a and 9b indicate the possible occurrence of a ductile shear zone along the dive track at water depths between 6000 and 6500 m. Such a shear zone would likely have a high dip angle and a normal and/or left-lateral sense of shear, probably having developed in conjunction with the West Santa Rosa Bank fault inferred by *Fryer et al.* [2003].

[27] Matrix olivine grains within the mylonitic peridotites are distinctly smaller than those within the porphyroclastic peridotites (compare R2 and R10 with R4, R5, and R7 in Figure 3), indicating that the two rock types formed under contrasting tectonic conditions [e.g., *Drury et al.*, 1991; *Michibayashi and Mainprice*, 2004]. Because finer grain size in olivine reflects higher flow stress [e.g., *Drury et al.*, 1991; *Jung and Karato*, 2001a], it is possible that the mylonitic peridotites developed at shallower levels and under lower-

Table 5. Electron Probe Analyses of Plagioclase of Dive 973 Peridotites[a]

	Sample Number					
	R02	R03	R04	R05	R06	R12
No. anal.	10	6	2	9	3	5
SiO_2	49.08	49.54	47.03	48.31	44.98	49.39
TiO_2	0.02	0.03	0.00	0.04	0.03	0.03
Al_2O_3	32.85	32.27	33.91	32.90	33.27	31.36
FeO	0.07	0.11	0.05	0.09	0.12	0.12
MnO	0.01	0.01	0.03	0.02	0.01	0.00
MgO	0.00	0.03	0.00	0.01	0.03	0.02
CaO	15.78	15.63	17.41	16.35	18.38	15.32
Na_2O	2.64	2.75	1.70	2.41	1.41	2.86
K_2O	0.01	0.00	0.00	0.01	0.01	0.01
Cr_2O_3	0.01	0.00	0.04	0.01	0.03	0.00
V_2O_3	0.01	0.01	0.01	0.01	0.00	0.01
NiO	0.01	0.00	0.02	0.00	0.02	0.01
P_2O_5	0.03	0.02	0.04	0.02	0.03	0.03
Total	100.53	100.39	100.25	100.19	98.33	99.15
Cations						
Si	2.23	2.25	2.16	2.21	2.11	2.28
Ti	0.00	0.00	0.00	0.00	0.00	0.00
Al	1.76	1.73	1.83	1.77	1.84	1.70
Fe	0.00	0.00	0.00	0.00	0.00	0.00
Mn	0.00	0.00	0.00	0.00	0.00	0.00
Mg	0.00	0.00	0.00	0.00	0.00	0.00
Ca	0.77	0.76	0.85	0.80	0.93	0.76
Na	0.23	0.24	0.15	0.21	0.13	0.26
K	0.00	0.00	0.00	0.00	0.00	0.00
Cr	0.00	0.00	0.00	0.00	0.00	0.00
V	0.00	0.00	0.00	0.00	0.00	0.00
Ni	0.00	0.00	0.00	0.00	0.00	0.00
P	0.00	0.00	0.00	0.00	0.00	0.00
O	8.00	8.00	8.00	8.00	8.00	8.00
Total	5.00	5.00	5.00	5.01	5.03	5.00
An	76.67	75.86	84.95	78.88	87.80	74.73
1σ	4.68	2.66	1.48	2.89	2.08	0.73
Ab	23.25	24.11	15.04	21.04	12.14	25.23
1σ	4.63	2.66	1.47	2.88	2.05	0.74
Or	0.08	0.03	0.01	0.08	0.06	0.03
1σ	0.07	0.02	0.01	0.05	0.08	0.04

[a] Unit is wt %. No. anal., number of analyses making up the average composition. An, anorthite content; Ab, albite content; Or, orthoclase content.

temperature conditions than the porphyroclastic peridotites. Alternatively, the different microstructures may result from the different degrees of deformation rather than a temperature differences [e.g., *Michibayashi et al.*, 2006a; *Warren et al.*, 2008]. We estimated temperature conditions assuming pressure of 10 kbar on the basis of Ca in orthopyroxene thermometer after *Brey and Köhler* [1990] (Figure 9c). Although estimated temperatures are in the range 800–1000°C, average temperatures from S1 to S4 are ~900°C despite variable microstructures (compare Figures 9a–9c), suggesting that estimated temperatures may not be directly related to their deformation conditions. Nonetheless, the coexistence of peridotites with contrasting microstructures (Figure 9a) may indicate a significant component of vertical displacement along the West Santa Rosa Bank fault zone, as required to exhume the observed peridotites and form scarps with up to 4 km of relief.

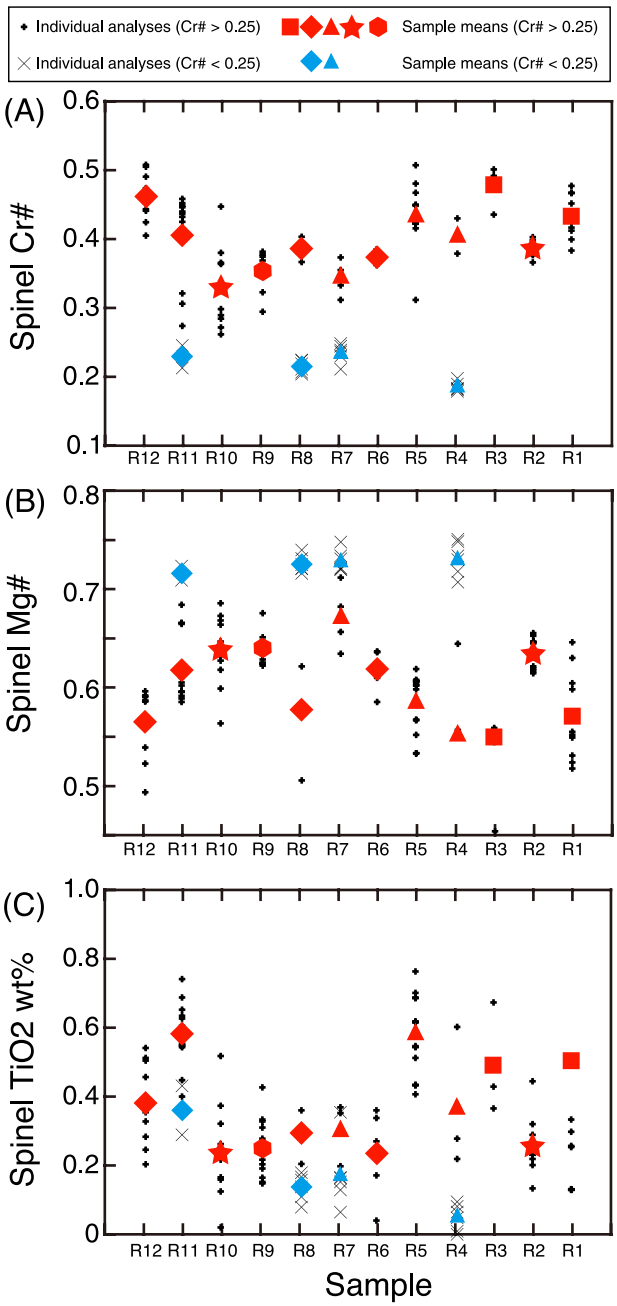

Figure 6. Mineral compositions for *Shinkai 6500* Dive 973 peridotites. (a) Spinel Cr #, (b) spinel Mg #, and (c) spinel TiO_2 wt %. Symbols for average compositions indicate petrographic characters, as in Figure 2b; red symbols correspond to samples with spinel Cr # > 0.25, and blue symbols show samples with spinel Cr # < 0.25.

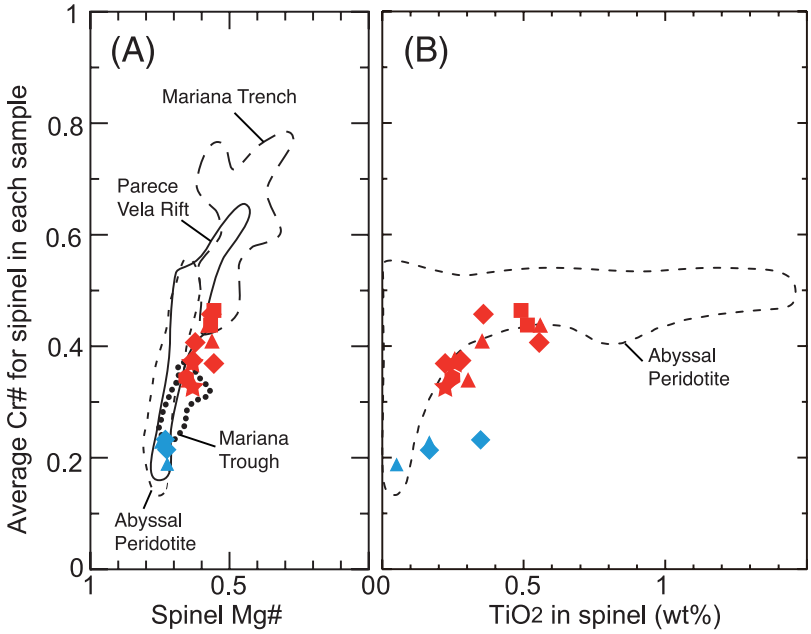

Figure 7. (a) Average Cr # versus average Mg # for spinel grains in each sample. Also shown are the fields for various oceanic peridotites: abyssal peridotite, *Dick and Bullen* [1984]; Mariana Trough, *Ohara et al.* [2002]; Parece Vela Rift, *Ohara et al.* [2003]; Mariana fore arc (landward slope of Mariana Trench), *Ohara and Ishii* [1998]. (b) Average Cr # versus average TiO_2 wt % for spinel grains in each sample. Also shown is the field for abyssal peridotite [*Dick and Bullen*, 1984]. Symbols are the same as those in Figure 6.

4.2. Petrological Characteristics

[28] Partial melting of the upper mantle and extraction of basaltic melts produces ultramafic tectonites as solid residues. The Cr # of spinel in abyssal peridotites is a useful indicator of the degree of melting [*Dick and Bullen*, 1984], with high-Cr # spinel generally representing depleted peridotite.

[29] The low-Cr # spinels (in R4, R7, R8 and R11) plot near the undepleted end of the global abyssal peridotite compositional array, whereas the high-Cr # spinels plot toward the more depleted end of the array (Figure 7a). Furthermore, in the Dive 973 sample suite, every sample except dunite (R9) includes plagioclase (as fresh grains and/or altered to hydrogrossular; e.g., Figure 4). Cr enrichment in spinel and the presence of plagioclase in peridotite has been explained by either (1) reequilibration of an ascending mantle body as it moves from spinel- to plagioclase-peridotite facies field through reaction, orthopyroxene + clinopyroxene + Al-spinel = olivine + plagioclase + Cr-spinel, or (2) impregnation of residual peridotite by either in situ or exotic melt through reaction, melt + Al-spinel = plagioclase + Cr-spinel [*Ohara et al.*, 2003, and references therein].

[30] The occurrence of low-Cr # and high-Cr # spinels within a single sample rules out the former mechanism, because remains of low-Cr # spinel could not have been preserved through this reaction. The high-Cr # spinels are enriched in incompatible elements such as Ti (Figure 7b), which is consistent with the idea that the Dive 973 sample suite represents melt-impregnated peridotite. We therefore interpret that the Dive 973 sample suite represents melt-impregnated peridotite.

[31] The composition of low-Cr # spinel is much more like the field of the Mariana Trough and/or Parece Vela Basin [*Ohara et al.*, 2002, 2003; *Ohara*, 2006] than the Mariana fore-arc peridotites [*Ishii et al.*, 1992; *Ohara and Ishii*, 1998], which are generally interpreted to have formed during the initiation of subduction [*Stern*, 2004] (Figure 7a). The low-Cr # spinels likely represent the intact composition of the residue of small degree of partial melting of a depleted MORB-type mantle beneath the Mariana Trough, which are left unaffected by the process of melt impregnation. The sample suite does not appear to be fragments of fore-arc mantle, in spite of the location of the sample site near the trench.

[32] Despite the fact that the Dive 973 sample suite was collected from the inner wall of the southern

Table 6. Bulk Rock Chemistry and Calculated Mineral Mode of Dive 973 Peridotites

	ID Number											
	R1	R2	R3	R4	R5	R6	R7	R8	R9	R10	R11	R12
	XRF (wt %), H_2O Free Basis											
SiO_2	45.10	45.73	45.45	45.39	44.86	46.67	46.09	46.40	43.70	45.27	45.18	46.53
TiO_2	0.053	0.101	0.103	0.079	0.077	0.073	0.070	0.054	0.007	0.040	0.054	0.052
Al_2O_3	2.37	3.10	3.98	2.74	2.79	2.50	2.69	2.30	0.63	1.42	2.39	2.53
Fe_2O_3	8.36	8.37	8.61	8.69	8.58	8.47	8.64	8.54	10.10	9.63	8.98	8.62
MnO	0.110	0.115	0.117	0.113	0.117	0.114	0.116	0.105	0.129	0.121	0.122	0.120
MgO	41.25	39.97	38.61	40.99	41.12	39.51	40.02	41.62	44.64	42.26	41.34	40.29
CaO	3.05	2.72	3.50	2.18	2.64	2.70	2.70	1.60	2.06	1.50	2.04	1.96
Na_2O	0.159	0.204	0.116	0.142	0.166	0.109	0.123	0.092	0.032	0.081	0.041	0.067
K_2O	0.017	0.014	0.019	0.020	0.015	0.022	0.024	0.018	0.027	0.018	0.015	0.023
P_2O_5	0.007	0.008	0.006	0.007	0.003	0.005	0.008	0.009	0.029	0.016	0.005	0.009
Total	100.47	100.34	100.51	100.34	100.36	100.18	100.48	100.74	101.34	100.36	100.16	100.19
LOI[a]	4.62	1.17	9.62	5.08	4.60	10.37	6.37	6.34	13.20	9.86	10.03	9.80
	XRF (ppm), H_2O Free Basis											
Cr	2488	2471	2910	2629	2709	2756	2661	2584	3343	3002	2645	2277
Ni	2269	2128	2094	2249	2171	2248	2229	2343	2751	2466	2344	2197
Sc	13.4	16.1	14.7	14.3	16.1	14.6	14.5	10.6	5.5	11.0	15.1	12.8
Sr	167.5	26.9	10.4	8.6	1.9	22.0	42.9	9.7	299.6	5.3	72.4	56.2
V	51.9	65.3	77.4	54.4	63.5	70.5	65.3	43.7	27.0	49.5	47.9	42.3
Y	2.0	3.4	3.1	1.7	3.1	2.9	3.0	1.8	0.2	1.4	1.2	1.4
Zr	Sr interference	4.5	3.7	2.6	2.6	1.7	3.6	2.6	Sr interference	1.5	2.0	2.6
	Calculated Mineral Mode											
Olivine	63.1 ± 2.0	65.1 ± 0.2	59.9 ± 2.2	60.2 ± 0.8	64.9 ± 0.5	50.9 ± 3.8	54.8 ± 3.5	56.8 ± 2.0		61.5 ± 2.1	61.4 ± 2.0	54.5 ± 3.1
Orthopyroxene	21.2 ± 2.8	20.1 ± 0.3	21.6 ± 2.9	29.3 ± 1.1	21.8 ± 0.7	36.2 ± 4.7	31.9 ± 4.4	36.6 ± 2.6		31.4 ± 3.1	29.3 ± 2.7	35.7 ± 4.2
Clinopyroxene	10.8 ± 2.0	9.2 ± 0.2	8.7 ± 1.8	5.2 ± 0.7	6.5 ± 0.5	7.3 ± 3.7	7.7 ± 3.4	3.8 ± 2.0		5.0 ± 1.8	4.4 ± 1.9	3.6 ± 2.6
Spinel	0.2 ± 1.0	0.8 ± 0.1	1.1 ± 1.0	0.4 ± 0.4	0.6 ± 0.3	0.4 ± 2.2	0.3 ± 2.0	0.3 ± 1.1		1.2 ± 0.8	0.5 ± 1.1	0.2 ± 1.5
Plagioclase	3.3 ± 1.2	6.1 ± 0.1	9.0 ± 1.2	3.5 ± 0.4	5.6 ± 0.3	2.9 ± 2.5	3.2 ± 2.4	1.5 ± 1.3		trace	2.9 ± 1.2	4.2 ± 1.8

[a] Loss on ignition.

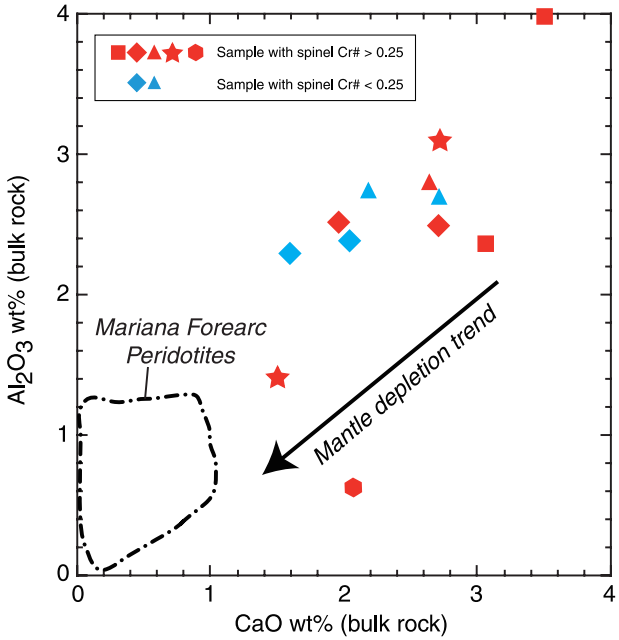

Figure 8. Al_2O_3 versus CaO diagram [after *Ishiwatari*, 1985], comparing data from the present study with those for the Mariana fore-arc (serpentinite diapir seamounts) peridotite [after *Ishii et al.*, 1992]. Symbols indicate petrographic characters, as in Figure 2b. Red symbols correspond to samples with spinel Cr # > 0.25, and blue symbols show samples with spinel Cr # < 0.25 (compare Figure 6a).

Mariana Trench (Figure 1), we argue that the sample suite formed in a tectonic environment that was more similar to that of a back-arc basin rather than a subduction initiation/fore-arc environment. The bulk rock chemistry further reveals that the sample suite is distinct from the fore-arc peridotites reported by *Ishii et al.* [1992, Table 4], instead lying on the less depleted end of the diagram (Figure 8).

4.3. Implications for Regional Tectonics

[33] *Fryer et al.* [2003] argued that north-south fore-arc deformation in the studied region resulted from slab rollback and trench retreat associated with a tear in the subducting plate, predicting left-lateral strike-slip shear above the slab tear. This proposal was supported by *Gvirtzman and Stern* [2004], who suggested that the lithosphere in the hanging wall adjacent to the Challenger Deep is as thin as 20 km. Such thin lithosphere could well have been intensely deformed during fore-arc extension [*Michibayashi et al.*, 2007], even perhaps in the ductile regime. Therefore, the development of the shear zone sampled by Dive 973 might be an upper plate response related to a tear in the subducting slab.

[34] Olivine CPO patterns within the analyzed peridotites indicate the dominance of [100](010) slip (Figure 5), suggesting development under

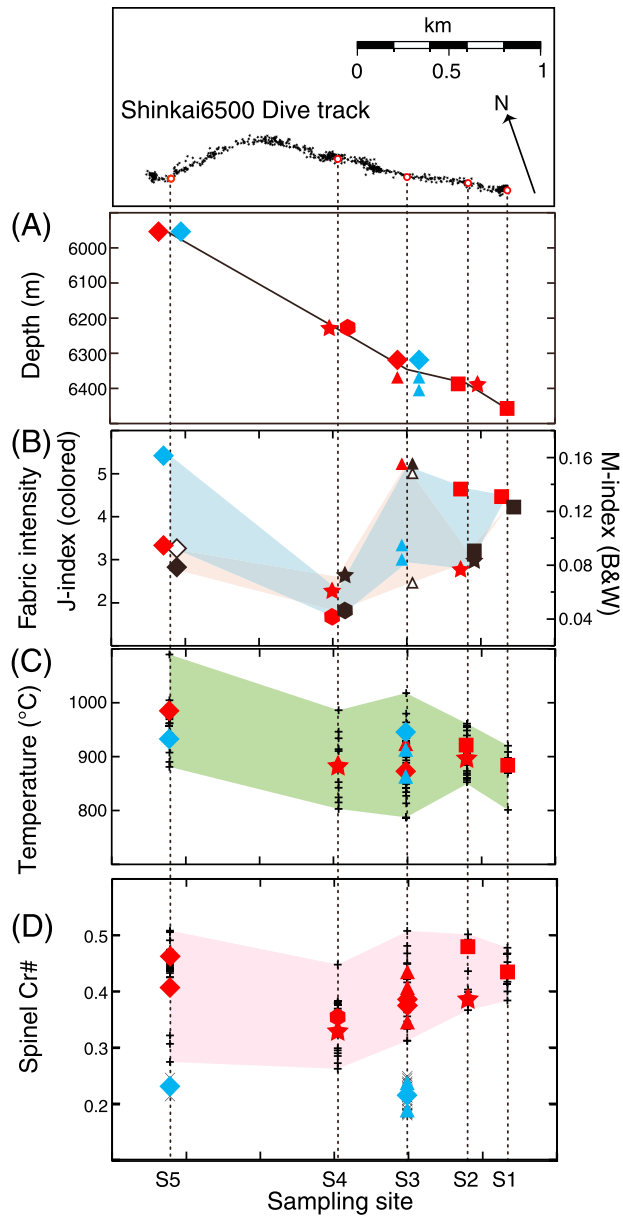

Figure 9. Spatial trends in deformation and mineral chemistry along the *Shinkai 6500* dive track. (a) Peridotite microstructure versus depth. The symbols are the same as those in Figure 8. (b) Olivine fabric intensity. J index values are shown with colored symbols that are the same as those in Figure 8, whereas M index values are shown with black (equal to the red) and white (equal to the blue) symbols. (c) Estimated temperature. The symbols are the same as those in Figure 8. (d) Spinel Cr #. The symbols are the same as those in Figure 6. See text for discussion.

anhydrous conditions [e.g., *Jung and Karato*, 2001b]. Given that the asthenospheric mantle is probably hydrated [*Michibayashi et al.*, 2007], these peridotites are likely to have been derived from the lithospheric mantle above the subducting slab, which may have formed from circulating asthenosphere following modest melt depletion. Moreover, the peridotites analyzed in this study have spinel and major element compositions that are characteristic of back-arc basin peridotites, especially those of the Mariana Trough [*Ohara et al.*, 2002]. Consequently, we infer that the origin of these peridotites was probably related to the development of the Mariana Trough back-arc basin at <7 Ma [e.g., *Stern et al.*, 2003].

5. Conclusions

[35] A dive made by the submersible *Shinkai 6500* (YK06–12 Dive 973) from the R/V *Yokosuka* in 2006 recovered peridotites from an eastward facing slope of the West Santa Rosa Bank fault at water depths of 6469–5957 m. The samples contain textures ranging from mylonitic to porphyroclastic to coarse-grained equigranular but moderately deformed. Crystal-preferred orientations of olivine within these peridotites dominantly show a distinct [100](010) pattern, although the fabric intensity decreases from rocks with coarse texture to mylonites. Consequently, the Dive 973 peridotites probably were derived from a large-scale ductile shear zone that developed within the overriding lithospheric mantle, presumably under anhydrous conditions and possibly above a tear in the subducting slab. The peridotites are now exposed along the N-S-striking West Santa Rosa Bank fault zone. Spinel compositions are compatible with those of peridotites from the Mariana Trough back arc, suggesting that typical fore-arc mantle is missing from this region, replaced by the back-arc basin mantle exposed along the West Santa Rosa Bank fault.

Acknowledgments

[36] We would like to thank the captain, crew, and scientists of the R/V *Yokosuka* and the *Shinkai 6500* team for their assistance and professional work. We are indebted to Susan Merle (NOAA-PMEL) for Figure 1 and to Eiichi Takazawa for providing a program to calculate the mineral modes in Table 6. Comments from the journal editor Peter van Keken and an associate editor and reviews by Eiichi Takazawa and Phillip Skemer improved the paper. K.M. acknowledges the help of Aaron Stallard in improving the English of the manuscript. This study was supported by research grants from the Japan Society for the Promotion of Science (16340151 and 19340148) awarded to K.M. and NSF grant OCE-0631365 awarded to R.J.S.

References

Bence, A. E., and A. L. Albee (1968), Empirical correction factors for the electron microanalysis of silicates and oxides, *J. Geol.*, *76*, 382–403.

Bird, P. (2003), An updated digital model of plate boundaries, *Geochem. Geophys. Geosyst.*, *4*(3), 1027, doi:10.1029/2001GC000252.

Brey, G. P., and T. Köhler (1990), Geothermobarometry in four-phase lherzolite II. New thermobarometers, and practical assessment of existing thermobarometers, *J. Petrol.*, *31*, 1353–1378.

Bunge, H. J. (1982), *Texture Analysis in Materials Sciences*, 593 pp., Butterworths, London.

Dick, H. J. B., and T. Bullen (1984), Chromian spinel as a petrogenetic indicator in abyssal and alpine-type peridotites and spatially associated lavas, *Contrib. Mineral. Petrol.*, *86*, 54–76, doi:10.1007/BF00373711.

Dijkstra, A. H., M. R. Drury, R. V. M. Vissers, and J. Newman (2002), On the role of melt-rock reaction in mantle shear zone formation in the Othris Peridotite Massif (Greece), *J. Struct. Geol.*, *24*, 1431–1450, doi:10.1016/S0191-8141(01)00142-0.

Drury, M. R., R. L. M. Vissers, and D. V. der Wal (1991), Shear localization in upper mantle peridotites, *J. Petrol.*, *137*, 439–460.

Fryer, P., N. Becker, B. Appelgate, F. Martinez, M. Edwards, and G. Fryer (2003), Why is the Challenger Deep so deep?, *Earth Planet. Sci. Lett.*, *211*, 259–269, doi:10.1016/S0012-821X(03)00202-4.

Fujioka, K., K. Okino, T. Kanamatsu, and Y. Ohara (2002), Morphology and origin of the Challenger Deep in the Southern Mariana Trench, *Geophys. Res. Lett.*, *29*(10), 1372, doi:10.1029/2001GL013595.

Gvirtzman, Z., and R. J. Stern (2004), Bathymetry of Mariana Trench-arc system and formation of the Challenger Deep as a consequence of weak plate coupling, *Tectonics*, *23*, TC2011, doi:10.1029/2003TC001581.

Harigane, Y., K. Michibayashi, and Y. Ohara (2005), Detachment faulting at the Godzilla Mullion, Parece Vela Basin, Philippine Sea, *Eos Trans. AGU*, *86*(52), Fall Meet. Suppl., Abstract T41D-1341.

Harigane, Y., K. Michibayashi, and Y. Ohara (2008), Shearing within lower crust during progressive retrogression: Structural analyses of gabbroic rocks from the Godzilla Mullion, an oceanic core complex in the Parece Vela backarc basin, *Tectonophysics*, *457*, 183–196, doi:10.1016/j.tecto.2008.06.009.

Ishii, T., P. T. Robinson, H. Maekawa, and R. Fiske (1992), Petrological studies of peridotites from diapiric serpentinite seamounts in the Izu-Ogasawara-Mariana forearc, Leg 125, *Proc. Ocean Drill. Program Sci. Results*, *125*, 593–614.

Ishiwatari, A. (1985), Igneous petrogenesis of the Yakuno Ophiolite (Japan) in the context of the diversity of ophiolites, *Contrib. Mineral. Petrol.*, *89*, 155–167, doi:10.1007/BF00379450.

Jaroslow, G. E., G. Hirth, and H. J. B. Dick (1996), Abyssal peridotite mylonites: Implications for grain-size sensitive flow and strain localization in the oceanic lithosphere, *Tectonophysics*, *256*, 17–37, doi:10.1016/0040-1951(95)00163-8.

Jung, H., and S. Karato (2001a), Effects of water on dynamically recrystallized grain size of olivine, *J. Struct. Geol.*, *23*, 1337–1344, doi:10.1016/S0191-8141(01)00005-0.

Jung, H., and S. Karato (2001b), Water-induced fabric transitions in olivine, *Science*, *293*, 1460–1463, doi:10.1126/science.1062235.

Karato, S. (2008), *Deformation of Earth Materials: An Introduction to the Rheology of Solid Earth*, 463 pp., Cambridge Univ. Press, Cambridge, U.K.

Kato, T., J. Beavan, T. Matsushima, Y. Kotake, J. Camacho, T. Jaun, and S. Nakao (2003), Geodetic evidence of backarc spreading in the Mariana Trough, *Geophys. Res. Lett.*, *30*(12), 1625, doi:10.1029/2002GL016757.

Kimura, J., and Y. Yamada (1996), Evaluation of major and trace element XRF analyses using a flux to sample ratio of two to one glass beads, *J. Mineral. Petrol. Econ. Geol.*, *91*, 62–72, doi:10.2465/ganko.91.62.

Mainprice, D. (2007), Seismic anisotropy of the deep Earth from a mineral and rock physics perspective, in *Treatise in Geophysics*, edited by G. Schubert, vol. 2, *Mineral Physics*, edited by G. D. Price, pp. 237–264, Elsevier, Amsterdam.

Mainprice, D., and P. G. Silver (1993), Interpretation of SKS-waves using samples from the subcontinental lithosphere, *Phys. Earth Planet. Inter.*, *78*, 257–280.

Mainprice, D., G. Barruol, and W. Ben Ismail (2000), The anisotropy of the Earth's mantle: from single crystal to polycrystal, in *Mineral Physics and Seismic Tomography: From Atomic to Global*, *Geophys. Monogr. Ser.*, vol. 117, edited by S. Karato et al., pp. 237–264, AGU, Washington, D.C.

Martinez, F., P. Fryer, and N. Becker (2000), Geophysical characteristics of the southern Mariana Trough, 11°50′N–13°40′N, *J. Geophys. Res.*, *105*, 16,591–16,607, doi:10.1029/2000JB900117.

Michibayashi, K. (2008), Structure sensitivity and elastic anisotropy within peridotites (in Japanese with the English abstract), *J. Geogr.*, *117*(1), 93–109.

Michibayashi, K., and D. Mainprice (2004), The role of pre-existing mechanical anisotropy on shear zone development within oceanic mantle lithosphere: An example from the Oman ophiolite, *J. Petrol.*, *45*, 405–414, doi:10.1093/petrology/egg099.

Michibayashi, K., T. Ina, and K. Kanagawa (2006a), The effect of dynamic recrystallization on olivine fabric and seismic anisotropy: Insights from a ductile shear zone in the Oman ophiolite, *Earth Planet. Sci. Lett.*, *244*, 695–708, doi:10.1016/j.epsl.2006.02.019.

Michibayashi, K., N. Abe, A. Okamoto, T. Satsukawa, and K. Michikura (2006b), Seismic anisotropy in the uppermost mantle, back-arc region of the northeast Japan arc: Petrophysical analyses of Ichinomegata peridotite xenoliths, *Geophys. Res. Lett.*, *33*, L10312, doi:10.1029/2006GL025812.

Michibayashi, K., M. Tasaka, Y. Ohara, T. Ishii, A. Okamoto, and P. Fryer (2007), Variable microstructure of peridotite samples from the southern Mariana Trench: Evidence of a complex tectonic evolution, *Tectonophysics*, *444*, 111–118, doi:10.1016/j.tecto.2007.08.010.

Miller, M. S., A. Gorbatov, and B. L. N. Kennet (2006), Three-dimensional visualization of a near-vertical slab tear beneath the southern Mariana arc, *Geochem. Geophys. Geosyst.*, *7*, Q06012, doi:10.1029/2005GC001110.

Newman, J., W. M. Lamb, M. R. Drudy, and R. L. M. Vissers (1999), Deformation processes in a peridotite shear zone: Reaction-softening by an H_2O-deficient, continuous net transfer reaction, *Tectonophysics*, *303*, 193–222, doi:10.1016/S0040-1951(98)00259-5.

Nicolas, A., and J. P. Poirier (1976), *Crystalline Plasticity and Solid State Flow in Metamorphic Rocks*, 444 pp., John Wiley, London.

Ohara, Y. (2006), Mantle process beneath Philippine Sea back-arc spreading ridges: A synthesis of peridotite petrology and tectonics, *Isl. Arc*, *15*, 119–129.

Ohara, Y., and T. Ishii (1998), Peridotites from the southern Mariana forearc: Heterogeneous fluid supply in mantle wedge, *Isl. Arc*, *7*, 541–558, doi:10.1111/j.1440-1738.1998.00209.x.

Ohara, Y., R. J. Stern, T. Ishii, H. Yurimoto, and T. Yamazaki (2002), Peridotites from the Mariana Trough: First look at the mantle beneath an active backarc basin, *Contrib. Mineral. Petrol.*, *143*, 1–18.

Ohara, Y., K. Fujioka, T. Ishii, and H. Yurimoto (2003), Peridotites and gabbros from the Parece Vela backarc basin: Unique tectonic window in an extinct backarc spreading ridge, *Geochem. Geophys. Geosyst.*, *4*(7), 8611, doi:10.1029/2002GC000469.

Ohara, Y., et al. (2006), Structure and composition of early arc crust: Observations and samples from Shinkai 6500 Dives in the southeastern Mariana Trench, *Eos Trans. AGU*, *87*(52), Fall Meet. Suppl., Abstract V41B-1709.

Skemer, P., I. Katayama, Z. Jiang, and S. Karato (2005), The misorientation index: Development of a new method for calculating the strength of lattice-preferred orientation, *Tectonophysics*, *411*, 157–167, doi:10.1016/j.tecto.2005.08.023.

Stern, R. J. (2004), Subduction initiation: Spontaneous and induced, *Earth Planet. Sci. Lett.*, *226*, 275–292.

Stern, R. J., and N. C. Smoot (1998), A bathymetric overview of the Mariana forearc, *Isl. Arc*, *7*, 525–540, doi:10.1111/j.1440-1738.1998.00208.x.

Stern, R. J., M. J. Fouch, and S. Klemperer (2003), An overview of the Izu-Bonin-Mariana Subduction Factory, in *Inside the Subduction Factory*, *Geophys. Monogr. Ser.*, vol. 138, edited by J. Eiler and M. Hirschmann, pp. 175–222, AGU, Washington, D.C.

Takazawa, E., T. Okayasu, and K. Satoh (2003), Geochemistry and origin of the basal lherzolites from the northern Oman ophiolite (northern Fizh block), *Geochem. Geophys. Geosyst.*, *4*(2), 8605, doi:10.1029/2001GC000232.

Tasaka, M., K. Michibayashi, and D. Mainprice (2008), B-type olivine fabrics developed in the fore-arc side of the mantle wedge along a subducting slab, *Earth Planet. Sci. Lett.*, *272*, 747–757, doi:10.1016/j.epsl.2008.06.014.

Warren, J. M., and G. Hirth (2006), Grain size sensitive deformation mechanisms in naturally deformed peridotites, *Earth Planet. Sci. Lett.*, *248*, 438–450, doi:10.1016/j.epsl.2006.06.006.

Warren, J. M., G. Hirth, and P. B. Kelemen (2008), Evolution of olivine lattice preferred orientation during simple shear in the mantle, *Earth Planet. Sci. Lett.*, *272*, 501–512, doi:10.1016/j.epsl.2008.03.063.

Webber, C. E., T. Little, J. Newman, and B. Tikoff (2008), Fabric superposition in upper mantle peridotite, Red Hills, New Zealand, *J. Struct. Geol.*, *30*, 1412–1428, doi:10.1016/j.jsg.2008.08.002.

Wheeler, J., D. Prior, Z. Jiang, R. Spiess, and P. Trimby (2001), The petrological significance of misorientations between grains, *Contrib. Mineral. Petrol.*, *141*, 109–124.